

Universal correlations in shallow D -wave systems

J. Braun^a, R. Roth^a, H.-W. Hammer^{a,b}

^aInstitut für Kernphysik, Technische Universität Darmstadt, 64289 Darmstadt, Germany

^bExtreMe Matter Institute EMMI, GSI Helmholtzzentrum für Schwerionenforschung GmbH, 64291 Darmstadt, Germany

Abstract

We investigate universal correlations between electromagnetic low-energy observables in systems with shallow D -wave states in the framework of Halo Effective Field Theory (Halo EFT). We propose a power counting scenario for weakly bound D -wave states in one-neutron halos and discuss its implications for universality. The scenario is applied to the $\frac{5}{2}^+$ first excited state and the $\frac{1}{2}^+$ ground state of ^{15}C . We obtain several universal correlations between electric observables and use experimental data for the E2 transition $\frac{5}{2}^+ \rightarrow \frac{1}{2}^+$ together with *ab initio* results from the No-Core Shell Model to predict the quadrupole moment at LO. We also discuss the effects of next-to-leading order (NLO) corrections for our results.

Keywords: Halo EFT, universality, D -wave states

1. Introduction

Weakly-bound quantum systems show universal properties independent of the details of their structure at short-distances [1]. Halo nuclei, which consist of a tightly bound core nucleus surrounded by one or more shallowly bound nucleons, display many universal aspects, such as a large radius and an extended tail of the wave function [2]. Exploiting the separation between the length scale of the core, R_{core} , and the length scale of the halo, R_{halo} , halo nuclei can be described using Halo Effective Field Theory (Halo EFT) [3, 4]. In this approach, the halo nucleus is described as an effective few-body system. The relevant degrees of freedom are the core and the halo nucleons. Halo EFT is complementary to *ab initio* nuclear structure methods that have difficulties describing weakly-bound states and provides a useful tool to identify universal correlations between observables. The input parameters of Halo EFT can either be taken from experiment or from *ab initio* calculations [5, 6, 7], which shows the versatility and the complementary character of halo EFT. Due to the weakly-bound nature of halo nuclei, different power-counting schemes are conceivable that exhibit a varying number of fine tuned parameters, especially for partial waves beyond S -wave states [3, 4]. In general, scenarios with a lower number of fine tunings are more likely to occur in nature, which favors the power counting proposed in Ref. [4] for P -wave states. Ultimately, the question of the power counting must be decided by comparison to experiment.

Halo EFT has been used to study various reactions and properties of halo systems. Initial studies in the strong sector have mainly focused on the universal properties of halo nuclei with S -wave [8, 9] and P -wave interactions [10, 11], including matter form factors and radii. In this paper, we focus on shallow D -wave states. In the context of the reaction $d + t \leftrightarrow n + \alpha$, D -wave states were previously considered in [12] using dimensional regularization with minimal subtraction. This procedure sets all power law divergences automatically to zero and thus

may miss some important contributions, as we will discuss below.

Electromagnetic observables provide a unique window to the structure and dynamics of halo nuclei. In Halo EFT, electromagnetic interactions can be straightforwardly included via minimal substitution and local gauge invariant operators in the effective Lagrangian [13]. Previous work focused on the electromagnetic structure and reactions of a variety of one- and two-neutron halos (see the review [14] for details) as well as on the general structure of proton halos [15, 16]. For general reviews of Halo EFT, see Refs. [17, 18, 14].

In this work, we extend the EFT for electromagnetic properties of S - and P -wave states presented in Ref. [13], to D -wave states. We apply this framework to ^{15}C , which has a $\frac{1}{2}^+$ ground state and an excited $\frac{5}{2}^+$ state. While the ground state is an S -wave state, the excited state is predominantly a D -wave bound state. We treat the strong D -wave interaction by introducing a new dimer field and compute electric form factors and the E2 transition strength. The electromagnetic form factors for the ground state of ^{15}C and the radiative neutron capture on ^{14}C to the $\frac{1}{2}^+$ ground state of ^{15}C were previously calculated in Refs. [19, 20]. The neutron separation energy of the $\frac{1}{2}^+$ state of ^{15}C is 1218 keV and the neutron separation energy of the $\frac{5}{2}^+$ state is 478 keV [21], while the first excitation of the ^{14}C nucleus is 6.1 MeV above the 0^+ ground state. This weak binding indicates a halo nature of the ground and first excited states of ^{15}C . Converting these energy scales into the relevant distance scales R_{core} and R_{halo} , we can estimate the EFT expansion parameter for this system as $R_{\text{core}}/R_{\text{halo}} \approx 0.3 - 0.4$.

The paper is organized as follows. After writing down the effective Lagrangian for the S - and D -wave case in Section 2, we calculate the dressed S - and D -wave propagators using the power divergence subtraction (PDS) scheme [22, 23]. We propose a power-counting scenario for the D -wave contributions and discuss its implications for universality. After electromag-

netic interactions are included in our theory, the electric form factors of the D -wave state and the B(E2) transition between the S - and D -wave state are calculated to leading order (LO) in Section 3. The next-to-leading order (NLO) corrections are also discussed. We identify a universal correlation between the B(E2) strength for the transition from the ground to the excited state and the quadrupole moment of the excited state μ_Q . We test this correlation in the case of ^{15}C . Our halo EFT results for ^{15}C are combined with experimental data for the B(E2) transition strength [21], and *ab initio* data from the importance-truncated no-core shell model (IT-NCSM) [24]. In this way, we are able to predict the quadrupole moment. We also compare our findings to correlations based on the simple rotational model by Bohr and Mottelson [25]. Similar correlations were previously identified in NCSM calculations of ^{12}C using chiral interactions [26]. In the case of ^{15}C , we provide an explanation based on the universality of shallow bound states. In Section 4, we present our conclusions.

2. Halo EFT formalism

Lagrangian. The relevant degrees of freedom are the ^{14}C core, a bosonic field c , and the halo neutron, a spin-1/2 field n . The strong S - and D -wave interactions are included through the incorporation of auxiliary spinor fields σ and d_{ij} , which correspond to the $\frac{1}{2}^+$ and $\frac{5}{2}^+$ states, respectively. Implicitly summing over repeated spin indices, the effective Lagrangian is written as:

$$\begin{aligned} \mathcal{L} = & \sum_{\phi=c,n} \phi^\dagger \left(i\partial_t + \frac{\nabla^2}{2m_\phi} \right) \phi + \sigma^\dagger \left[\eta_0 \left(i\partial_t + \frac{\nabla^2}{2M_{nc}} \right) + \Delta_0 \right] \sigma \\ & + d_{ij}^\dagger \left[c_2 \left(i\partial_t + \frac{\nabla^2}{2M_{nc}} \right)^2 + \eta_2 \left(i\partial_t + \frac{\nabla^2}{2M_{nc}} \right) + \Delta_2 \right] d_{ij} \\ & - g_0 \left[c^\dagger n^\dagger \sigma + \text{h.c.} \right] - g_2 \left[d_{ij}^\dagger \left(n \overleftrightarrow{D}_{ij} c \right) + \text{h.c.} \right] \end{aligned} \quad (1)$$

where spin-1/2 indices are suppressed, $i, j \in \{1, 2, 3\}$ are vector indices, m_n denotes the neutron mass, m_c the core mass and $M_{nc} = m_n + m_c$ is the total mass of the neutron-core system.

The Cartesian form of the strong D -wave interaction is taken from Refs. [4, 12]:

$$D_{ij}^2 = \frac{1}{2} \left(\overleftrightarrow{\nabla}_i \overleftrightarrow{\nabla}_j + \overleftrightarrow{\nabla}_j \overleftrightarrow{\nabla}_i \right) - \frac{1}{D-1} \overleftrightarrow{\nabla}^2 \delta_{ij}, \quad (2)$$

where D denotes the spacetime dimension and $\overleftrightarrow{\nabla}_j$ is a Galilei-invariant derivative. The D -wave interaction yields 9 terms, but only 5 of them are linear independent, corresponding to the 5 components of a D -wave state. The Lagrangian (2) exhibits all relevant symmetries. In particular, the D -wave part is symmetric under permutation of the indices i and j , which preserves gauge invariance after the inclusion of photons via minimal substitution. For the D -wave we have four constants in our Lagrangian: c_2, η_2, Δ_2 and g_2 , but only three of them are linearly independent. We are free to set one to a fixed value. Here, we

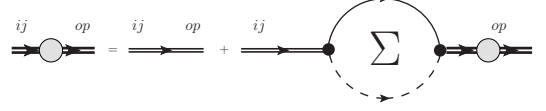


Figure 1: Diagrammatic representation of the dressed D -wave propagator. The dashed (solid) line denotes the core (neutron) field. The thin double line represents the bare dimer propagator, while the thick double line with the blob is the dressed dimer propagator.

choose $\eta_2 = \pm 1$, where the overall sign sets the sign of the D -wave effective range. The term proportional to c_2 [27] is then needed to absorb the scale dependence from loop corrections.

S-wave propagator. The dressed propagators of the σ and d_{ij} fields are obtained by summing the bubble diagrams for the nc -interactions (cf. Fig. 1) to all orders. The σ -propagator for the S -wave state is well known (see, e.g., Ref. [13]) and we quote only the final result:

$$D_\sigma(\tilde{p}_0) = \frac{1}{\Delta_0 + \eta_0[\tilde{p}_0 + i\epsilon] - \Sigma_\sigma(\tilde{p}_0)}, \quad (3)$$

$$\Sigma_\sigma(\tilde{p}_0) = -\frac{g_0^2 m_R}{2\pi} \left[i\sqrt{2m_R \tilde{p}_0} + \mu \right], \quad (4)$$

where μ is the PDS scale [22, 23], m_R the reduced mass of the neutron-core system, and $\tilde{p}_0 = p_0 - \mathbf{p}^2/(2M_{nc})$ is the Galilei invariant energy.

D-wave propagator. The dressed propagator for the d_{ij} field can be computed from the diagrams in Fig. 1. Since we use a Cartesian representation of the D -wave, the dressed propagator depends on four vector indices, two in the incoming channel and two in the outgoing channel. Evaluating the Feynman diagrams in Fig. 1, we obtain:

$$D_d(\tilde{p}_0)_{ij,op} = D_d(\tilde{p}_0) \frac{1}{2} \left(\delta_{io} \delta_{jp} + \delta_{ip} \delta_{jo} - \frac{2}{3} \delta_{ij} \delta_{op} \right), \quad (5)$$

$$D_d(\tilde{p}_0) = \left[\Delta_2 + \eta_2 \tilde{p}_0 + c_2 \tilde{p}_0^2 - \Sigma_d(\tilde{p}_0) \right]^{-1}, \quad (6)$$

with the one-loop self-energy

$$\Sigma_d(\tilde{p}_0) = -\frac{2}{15} \frac{m_R g_2^2}{2\pi} (2m_R \tilde{p}_0)^2 \left[i\sqrt{2m_R \tilde{p}_0} + i\epsilon - \frac{15}{8} \mu \right]. \quad (7)$$

The D -wave scattering amplitude in the two-body center-of-mass frame with $E = k^2/(2m_R)$ and $k = |\mathbf{p}'| = |\mathbf{p}|$ for on-shell scattering

$$t_2(\mathbf{p}', \mathbf{p}; E) = g_2^2 \left[(\mathbf{p} \cdot \mathbf{p}')^2 - \frac{1}{3} \mathbf{p}^2 \mathbf{p}'^2 \right] D_d(E, \mathbf{0}), \quad (8)$$

is matched to the effective range expansion

$$t_2(\mathbf{p}', \mathbf{p}; E) = \frac{15\pi}{m_R} \frac{(\mathbf{p} \cdot \mathbf{p}')^2 - \frac{1}{3} \mathbf{p}^2 \mathbf{p}'^2}{1/a_2 - \frac{1}{2} r_2 k^2 + \frac{1}{4} \mathcal{P}_2 k^4 + ik^5}, \quad (9)$$

and we find the conditions

$$\frac{1}{a_2} = \frac{15\pi}{m_R g_2^2} \Delta_2, \quad r_2 = -\frac{15\pi}{m_R^2 g_2^2} \eta_2, \quad \mathcal{P}_2 = \frac{15\pi}{m_R^3 g_2^2} c_2 + \frac{15}{2} \mu. \quad (10)$$

The term proportional to c_2 in (1) is required to absorb the μ -dependence from the PDS scheme. As a consequence, the terms proportional to η_2 , Δ_2 , and g_2 are also required to be consistent with the threshold expansion of the scattering amplitude. All couplings can be fixed from the effective range parameters a_2 , r_2 , and \mathcal{P}_2 if they are known. This pattern motivates the power-counting scheme discussed below.

Power counting. The canonical power counting for the $D_\sigma(p)$ propagator representing a shallow S -wave state was given in Refs. [28, 29, 22, 23]. It implies $1/\gamma_0 \sim a_0 \sim R_{\text{halo}}$ and $r_0 \sim R_{\text{core}}$, where γ_0 is the binding momentum of the S -wave state and r_0 the effective range. As a result, r_0 enters at NLO in the expansion in $R_{\text{core}}/R_{\text{halo}}$. For the specific case of ^{15}C , Fernando et al. [19] argued that effective range corrections could be large, $r_0\gamma_0 \sim 0.6$, such that it would be more appropriate to count $r_0 \sim R_{\text{halo}}$ and thus keep it at LO. The extracted value for $r_0 = 2.67 \text{ fm}$ [19] results from a fit to one-neutron capture data $^{14}\text{C}(n, \gamma)^{15}\text{C}$ [30]. We follow this suggestion and treat r_0 as an LO parameter for ^{15}C .

The power counting for partial waves beyond the S -wave is more complicated and different scenarios have been proposed [3, 4]. We apply the constraint to exhibit the minimal number of fine tunings possible in our power-counting scheme. This is motivated by the fact that every additional fine tuning makes the scenario less likely to be found in nature. Bedaque et al. [4] suggest for the P -wave case that $a_1 \sim R_{\text{halo}}^2 R_{\text{core}}$ and $r_1 \sim 1/R_{\text{core}}$, where higher ERE parameters scale with the appropriate power of R_{core} . This requires only one fine-tuned constant in \mathcal{L} instead of two as proposed in Ref. [3] where both a_1 and r_1 scale only with R_{halo} . The P -wave power counting in [4] was also generalized to $l > 1$. However, we find that the number of fine tunings for $l = 2$ is larger than proposed in Ref. [4] since a_2 , r_2 , and \mathcal{P}_2 are all needed at LO for the D -wave. In the case of the $D_d(p)$ propagator, (5), two out of three ERE parameters need to be fine-tuned because $a_2 \sim R_{\text{halo}}^4 R_{\text{core}}$ and $r_2 \sim 1/(R_{\text{halo}}^2 R_{\text{core}})$ are both unnaturally large. In addition, we adopt $\mathcal{P}_2 \sim 1/R_{\text{core}}$ for the μ -independent part in Eq. (10) and count $\mu \sim 1/R_{\text{halo}}$, which thus contributes at NLO. Higher ERE terms are suppressed by powers of $R_{\text{core}}/R_{\text{halo}}$. Thus, the relevant fit-parameters in our EFT at LO are γ_0 , r_0 , γ_2 , r_2 , and \mathcal{P}_2 , where γ_2 is the binding momentum of the D -wave state. The corresponding wave function renormalization constants at LO are:

$$Z_\sigma = \frac{2\pi}{m_R^2 g_0^2} \frac{\gamma_0}{1 - r_0 \gamma_0}, \quad Z_d = -\frac{15\pi}{m_R^2 g_2^2} \frac{1}{r_2 + \mathcal{P}_2 \gamma_2^2}. \quad (11)$$

As pointed out in the introduction, the interacting D -wave propagator was already calculated in the context of the $d + t \leftrightarrow n + \alpha$ reaction in Ref. [12], where the coupling of the unstable particle field to the αn pair with spin $3/2$ involves an internal D -wave angular momentum. Employing a similar approach for the coupling of the cn pair we obtain the same Cartesian tensor structure as in Eq. (5).

We note that in Ref. [12], the minimal subtraction (MS) scheme [31, 32] is used, which subtracts poles in $D = 4$ dimensions. In PDS, in contrast, the poles in $D = 4$ and $D = 3$ are both subtracted. If there are no poles in $D = 3$, PDS and MS

yield the same result. In the calculation of the self-energy for the D -wave propagator, (5), there is only a pole in $D = 3$. As a consequence, no subtractions are required in MS. However, as argued in Refs. [22, 23], the MS scheme is not well suited for systems with shallow bound states where the tracking of power law divergences is important. In the case of the D -wave propagator, the contributions of r_2 and \mathcal{P}_2 are missed.

Electromagnetic interactions. Electromagnetic interactions are included via minimal substitution in the Lagrangian $\partial_\mu \rightarrow D_\mu = \partial_\mu + ie\hat{Q}A_\mu$, where the charge operator \hat{Q} acting on the ^{14}C core yields $\hat{Q}c = 6c$. In addition to the electromagnetic interactions resulting from the application of the minimal substitution in the Lagrangian, we have to consider local gauge-invariant operators involving the electromagnetic field $A^\mu = (A_0, \mathbf{A})$ and the fields c , n , σ and d_{ij} . Depending on the observable and respective partial wave, they contribute at different orders of our EFT. The local operators with one power of the photon field, relevant in our LO calculation of electric form factors and the $B(E2)$ transition strength, are:

$$\begin{aligned} \mathcal{L}_{EM} = & -L_{C0}^{(\sigma)} \sigma^\dagger \sigma (\nabla^2 A_0) - L_{C01}^{(d)} d_{ij}^\dagger d_{ij} (\nabla^2 A_0) + \dots \\ & - L_{C02}^{(d)} d_{ij}^\dagger d_{op} \left(\nabla_i \nabla_o \delta_{jp} - \frac{\nabla_i \nabla_j \delta_{op}}{3} - \frac{\nabla_o \nabla_p \delta_{ij}}{3} + \frac{\delta_{op} \delta_{ij}}{9} \right) A_0, \end{aligned} \quad (12)$$

where we have omitted the contributions from \mathbf{A} .

To determine the order at which they occur we follow the procedure from Ref. [27, 13]. The d_{ij} and σ fields are rescaled so that they absorb factors of g_0 , g_2 and m_R and have non-canonical dimensions:

$$\tilde{d}_{ij} = d_{ij} g_2 m_R, \quad \tilde{\sigma} = \sigma g_0 m_R. \quad (13)$$

For the rescaled σ field we extract the non-canonical dimension from Ref. [13]: $[\tilde{\sigma}] = 2$. To identify how $g_2 m_R$ scales with R_{core} we reconsider the matching to the effective range expansion of the D -wave propagator. Equation (10) yields:

$$g_2^2 m_R^2 \sim 15\pi / r_2, \quad (14)$$

and thus, we find the non-canonical dimension $[\tilde{d}_{ij}] = 0$ for the rescaled field. Using naive dimensional analysis, we can now determine the scaling of the operators with respect to R_{core} . As a result, the coefficients written above scale as:

$$L_{C0}^{(\sigma)} \sim R_{\text{core}}^3 l_{C0}^{(\sigma)} g_0^2 m_R^2, \quad (15)$$

$$L_{C01}^{(d)} \sim R_{\text{core}}^{-1} l_{C01}^{(d)} g_2^2 m_R^2, \quad (16)$$

$$L_{C02}^{(d)} \sim R_{\text{core}}^{-1} l_{C02}^{(d)} g_2^2 m_R^2, \quad (17)$$

with parameters l_{\dots} all of order one. In the next section, we show that the operators $\sim L_{C01}^{(d)}$ and $L_{C02}^{(d)}$ contribute already at LO.

3. EM observables

In this section, we use the Lagrangian (1) with minimal substitution plus the local, gauge-invariant operators (12) to compute the D -wave form factors and the strength of the $E2$ transition from the $\frac{1}{2}^+$ to the $\frac{5}{2}^+$ state at LO. Some preliminary results were already presented in Ref. [33].

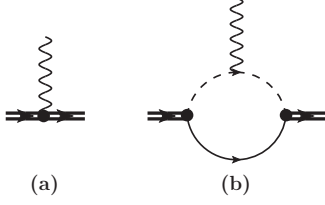


Figure 2: The topologies contributing to the irreducible vertex for an A_0 photon to couple to the nc D -wave bound state field up to NLO.

Form factors. The result for the electric form factor of an S -wave one-neutron halo is given in Refs. [13, 19] for ^{11}Be and ^{15}C . The experimental result for the rms charge radius of ^{14}C is $\langle r_E^2 \rangle_{^{14}\text{C}}^{1/2} = 2.5025(87) \text{ fm}$ [34] and the halo EFT result for the $\frac{1}{2}^+$ S -wave ground state is $\langle r_E^2 \rangle_{^{15}\text{C}}^{(\sigma)} \approx 0.11 \text{ fm}^2$ [19] but the authors do not quote an error for this number. In principle, both values can be combined to obtain a prediction for the full charge radius of the ^{15}C ground state.

Here, we focus on the properties of the excited $\frac{5}{2}^+$ D -wave state. We follow [13] and compute the form factors of the D -wave state by calculating the contribution to the irreducible vertex for $A_0 dd$ interactions up to NLO shown in Fig. 2.

The first topology represents three different direct couplings of the photon to the d_{ij} field. Two couplings emerge from the minimal substitution in Eq. (1) since r_2 and \mathcal{P}_2 contribute at LO. The last one are the counterterms $\sim L_{C01/2}^{(d)}$ entering at LO which arise from Eq. (12). The second diagram arises from minimal substitution in the strong D -wave interaction in Eq. (1) and contributes only at NLO. The computation is carried out in the Breit frame, $q = (0, \mathbf{p}' - \mathbf{p})$, and yields the electric $G_E(|\mathbf{q}|)$, quadrupole $G_Q(|\mathbf{q}|)$ and hexadecupole $G_H(|\mathbf{q}|)$ form factors. At LO only topology (a) contributes, and we find:

$$G_E(|\mathbf{q}|) = \frac{1}{r_2 + \mathcal{P}_2 \gamma_2^2} \left[\left(\tilde{L}_{C01}^{(d)\text{LO}} + \frac{4}{3} \tilde{L}_{C02}^{(d)\text{LO}} \right) |\mathbf{q}|^2 + \gamma_2^2 \mathcal{P}_2 + r_2 \right], \quad (18)$$

$$G_Q(|\mathbf{q}|) = \frac{2M_{nc}^2}{r_2 + \mathcal{P}_2 \gamma_2^2} \left[\frac{20}{3} \tilde{L}_{C02}^{(d)\text{LO}} \right], \quad (19)$$

$$G_H(|\mathbf{q}|) = 0, \quad (20)$$

At NLO both topologies, Fig. 2(a) and (b), contribute and (b) yields a LO contribution to $G_H(|\mathbf{q}|)$. This will be considered in a subsequent publication [35]. The neutron spin is unaffected by the charge operator up to the order considered here. The local gauge-invariant operators $\sim L_{C01/2}^{(d)}$ contribute at LO. It is convenient to define

$$\tilde{L}_{C01/2}^{(d)\text{LO}} = \frac{15\pi}{eQ_c g_2^2 m_R^2} L_{C01/2}^{(d)\text{LO}}, \quad (21)$$

which scales as R_{core}^{-1} .

The electric form factor for $|\mathbf{q}| \rightarrow 0$ is normalized such that:

$$G_E(|\mathbf{q}|) \approx 1 - \frac{1}{6} \langle r_E^2 \rangle |\mathbf{q}|^2 + \dots, \quad (22)$$

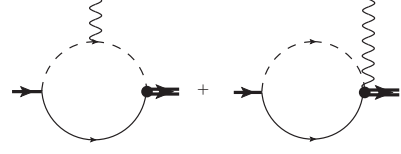


Figure 3: The two LO diagrams contributing to the irreducible vertex that determines the S -to- D state transition in halo EFT. The thick double line denotes the dressed D -wave propagator and the thick single line the dressed S -wave propagator.

and an expansion of Eq. (18) yields $G_E(0) = 1$ and an electric radius of the D -wave state at LO:

$$\langle r_E^2 \rangle^{(d)} = -\frac{6\tilde{L}_{C0E}^{(d)\text{LO}}}{r_2 + \mathcal{P}_2 \gamma_2^2}, \quad (23)$$

where we have defined $\tilde{L}_{C0E}^{(d)\text{LO}} = \tilde{L}_{C01}^{(d)\text{LO}} + \frac{4}{3}\tilde{L}_{C02}^{(d)\text{LO}}$. The loop diagram in Fig. 2(b) is suppressed by one power of $R_{\text{core}}/R_{\text{halo}}$ and contributes at NLO.

From the expression for the quadrupole form factor, Eq. (19), we can read off the quadrupole moment via, $G_Q(|\mathbf{0}|) = M_{nc}^2 \mu_Q$, and obtain

$$\mu_Q^{(d)} = \frac{40\tilde{L}_{C02}^{(d)\text{LO}}}{3(r_2 + \mathcal{P}_2 \gamma_2^2)}. \quad (24)$$

We cannot give numerical values for the charge radius of the D -wave state since the relevant ERE parameters are unknown and there is no experimental data to match the counterterm $\tilde{L}_{C0E}^{(d)\text{LO}}$ which enters already at LO in the D -wave case.

E2 transition. The diagrams contributing to the irreducible vertex for the E2 transition from the $\frac{1}{2}^+$ state to the $\frac{5}{2}^+$ state at LO are shown in Fig. 3. The photon has a four momentum of $k = (\omega, \mathbf{k})$. We calculate the irreducible vertex in Coulomb Gauge so that we have $\mathbf{k} \cdot \epsilon = 0$ for real photons. Additionally, we choose $\mathbf{k} \cdot \mathbf{p} = 0$, where \mathbf{p} denotes the incoming momentum of the S -wave state. As a result, the space-space components of the vertex function in Cartesian coordinates can be written as:

$$\tilde{\Gamma}_{ijk} = \Gamma_E \frac{1}{2} (k_j \delta_{ik} + k_i \delta_{jk}) + \Gamma_M p_k \left(k_i k_j - \frac{1}{3} \delta_{ij} k^2 \right). \quad (25)$$

By choosing the photon to be traveling in the \hat{z} direction, we obtain $\tilde{\Gamma}_{333} = \Gamma_E \omega$, with $|\mathbf{k}| = k_3 = \omega$. Comparing the definitions for the transition rate depending on B(E2) and the transition rate as a function of the irreducible vertex Γ_E [36] we get:

$$\text{B(E2)} = \frac{15}{\pi} \frac{1}{k^4} |\Gamma_{m'm_s\mu}|^2, \quad (26)$$

where m' denotes the total angular momentum projection of the $\frac{5}{2}^+$ state, m_s is the spin projection of the $\frac{1}{2}^+$ state and μ denotes the photon polarization. Since the neutron spin is unaffected by this transition, we calculate the vertex function with respect to the specific components of the D -wave interaction. In the case of $m_s = m' = \pm 1/2$ only $m_l = 0$ contributes and we get:

$$\Gamma_{\pm\pm 3} = \left(\frac{1}{2} \pm \frac{1}{2} \right) 20 \left| \frac{5}{2} \pm \frac{1}{2} \right\rangle (10 \ 10 \ 20) \tilde{\Gamma}_{333} = \sqrt{\frac{2}{5}} \Gamma_E \omega, \quad (27)$$

where \pm denotes the total angular momentum projection $\pm 1/2$. Replacing $\Gamma_{m'm_s\mu}$ in Eq. (26) with Eq. (27), we have:

$$B(E2) = \frac{15}{\pi} \left(\frac{\Gamma_{++3}}{\omega^2} \right)^2 = \frac{6}{\pi} \left(\frac{\tilde{\Gamma}_E}{\omega} \right)^2, \quad (28)$$

with the renormalized, irreducible vertex $\tilde{\Gamma}_E = \sqrt{Z_\sigma Z_d} \Gamma_E$. At LO, Z_σ and Z_d are given in Eq. (11). Using the result of our calculation for Γ_E , we find for the transition $\frac{1}{2}^+ \rightarrow \frac{5}{2}^+$:

$$B(E2) = \frac{6}{15\pi} \frac{Z_{eff}^2 e^2}{r_2 + \mathcal{P}_2 \gamma_2^2} \frac{-\gamma_0}{1 - r_0 \gamma_0} \left[\frac{3\gamma_0^2 + 9\gamma_0 \gamma_2 + 8\gamma_2^2}{(\gamma_0 + \gamma_2)^3} \right]^2, \quad (29)$$

where the effective charge for ^{15}C , $Z_{eff} = (m/M_{nc})^2 Q_c \approx 0.027$ [37], comes out of the calculation automatically. The renormalized $B(E2)$ matrix element scales as $R_{halo} \sqrt{R_{core}} R_{halo}$. To this order there are no counterterms but at NLO there is a short-range contribution to the transition [35].

As usual, the same result for $\tilde{\Gamma}_E$ can be obtained using current conservation,

$$\omega \tilde{\Gamma}_{ij0} = k_k \tilde{\Gamma}_{ijk}, \quad (30)$$

if we calculate the space-time components of the vertex function $\tilde{\Gamma}$. In contrast to $\tilde{\Gamma}_{ijk}$, we have to consider only the left diagram in Fig. 2 for $\tilde{\Gamma}_{ij0}$.

Correlations between E2 observables. Up to this point, all the results are universal and not specific for ^{15}C . In this section, we combine our halo EFT results with experimental data and *ab initio* data from the IT-NCSM [24] to predict electric properties for ^{15}C . In a second step, the correlations obtained in halo EFT are compared to the E2 correlation based on the rotational model by Bohr and Mottelson [25].

The experimental result for the E2 strength for the transition $5/2^+ \rightarrow 1/2^+$ in ^{15}C is $B(E2) = 0.44(1)$ W.u. [21]. This yields $B(E2) = 2.90(7) e^2 \text{fm}^4$ for the transition $1/2^+ \rightarrow 5/2^+$ we have calculated above. For the binding momentum we obtain $\gamma_0 = 0.235 \text{ fm}^{-1}$ and $\gamma_2 = 0.147 \text{ fm}^{-1}$ [21] and $r_0 = 2.67 \text{ fm}$ [19]. From these numbers one can extract $Z_d \sim 1/(r_2 + \mathcal{P}_2 \gamma_2^2) = -362(8) \text{ fm}^3$, and using Eq. (23), $\langle r_E^2 \rangle^{(d)} = -2176(50) \tilde{L}_{C0E}^{(d) \text{ LO}} \text{ fm}^3$. Additionally, we find $\mu_Q^{(d)} = -4836(110) \tilde{L}_{C02}^{(d) \text{ LO}} \text{ efm}^3$.

With the numerical result for Z_d we can check if our power-counting scenario, leading to the scaling $Z_d \sim R_{halo}^2 R_{core}$, can be confirmed or if the scenario of [4] yields better agreement. An approximation for the halo scale can be extracted from the neutron separation energy S_n , $R_{halo} \approx 1/\gamma_2 = 1/\sqrt{S_n 2m_R} = 6.81 \text{ fm}$. We can approximate the core radius by looking at the energy of the first excitation of the ^{14}C nucleus $E_{ex} = 6.1 \text{ MeV}$. Converting this energy into a length scale we obtain $R_{core} \approx 1.91 \text{ fm}$. By employing the experimental values for R_{halo} and R_{core} we predict $Z_d \sim R_{halo}^2 R_{core} \approx 90 \text{ fm}^3$. This value is by a factor of 4 smaller than the one extracted from $B(E2)$ and thus in reasonable agreement. The power counting of [4] does lead to the scaling $Z_d = 1/r_2 \sim R_{core}^3 \approx 7 \text{ fm}^3$ which is around 52

times smaller than the extracted result. These numbers indicate that our power-counting scenario is better suited for ^{15}C .

To obtain the correlation between the the quadrupole transition from the $\frac{5}{2}^+$ state to the $\frac{1}{2}^+$ state and the quadrupole moment of the $\frac{5}{2}^+$ state, we combine Eqs. (24) and (29) and apply a factor $2/6$ to account for the different multiplicity of initial and final states. We obtain a linear dependence between $B(E2)$ for the transition $\frac{5}{2}^+ \rightarrow \frac{1}{2}^+$ and the quadrupole moment:

$$B(E2) = \frac{-1}{100\pi} \frac{Z_{eff}^2 e^2 \gamma_0}{(1 - r_0 \gamma_0)} \left[\frac{3\gamma_0^2 + 9\gamma_0 \gamma_2 + 8\gamma_2^2}{(\gamma_0 + \gamma_2)^3} \right]^2 \frac{\mu_Q^{(d)}}{\tilde{L}_{C02}^{(d) \text{ LO}}}, \quad (31)$$

where $\tilde{L}_{C02}^{(d) \text{ LO}}$ is treated as fit parameter and γ_0 and γ_2 are taken from experiment [21].

A similar correlation between the quadrupole transition and the quadrupole moment can be obtained from the rotational model by Bohr and Mottelson [25]:

$$B(E2, J_i \rightarrow J_f) = \frac{5}{16\pi} \frac{((J+1)(2J+3))^2}{(3K^2 - J(J+1))^2} \times (J_i K \ 20 | J_f K)^2 \left(\frac{Q_{0,t}}{Q_{0,s}} \right)^2 \mu_Q(J)^2, \quad (32)$$

where $K = 1/2$ denotes the projection of the total angular momentum on the symmetry axis of the intrinsically deformed nucleus and $Q_{0,t}/Q_{0,s}$ is the ratio between intrinsic static (s) and transition (t) quadrupole moment in the rigid rotor model. The idea to employ this simple model is motivated by observations of Calci and Roth [26], who found a robust correlation between this pair of quadrupole observables in *ab initio* calculations for light nuclei. In the simple rigid rotor model the ratio $Q_{0,t}/Q_{0,s}$ is expected to be one. The results of Ref. [26] indicate that the correlation is robust as long as the ratio $Q_{0,t}/Q_{0,s}$ is treated as a fit parameter.

We use IT-NCSM data of ^{15}C to check the quadratic and linear correlations and predict numerically the quadrupole moment of ^{15}C . This is demonstrated in Fig. 4. The data we employ for the fit is different in both plots. The varying symbols denote different $NN+3N$ chiral EFT interactions which are similar to the ones used in Ref. [26]. We use the NN interaction developed by Entem and Machleidt (EM) [38] at $N^3\text{LO}$ with a cutoff of 500 MeV/c for the nonlocal regulator function. This NN force is combined with the local 3N force at $N^2\text{LO}$ using a cutoff of 400 or 500 MeV/c [39]. The second NN interaction by Epelbaum, Glöckle, Meißner (EGM) [40] at $N^2\text{LO}$ uses a non-local regularization with a cutoff $\tilde{\Lambda}_\chi$ and an additional spectral function regularization with cutoff $\tilde{\Lambda}_\chi$. The EGM NN forces are combined with a consistent nonlocal 3N force at $N^2\text{LO}$ used in several applications to neutron matter [41, 42, 43]. For reasons of convergence, the $NN + 3N$ potentials are softened by a similarity renormalization group evolution where all contributions up to the three-body level are included. The different colors in Fig. 4 denote different N_{max} values. Since the IT-NCSM results are not fully converged, the ordering of the ground and first excited state is exchanged for some data points. Leaving

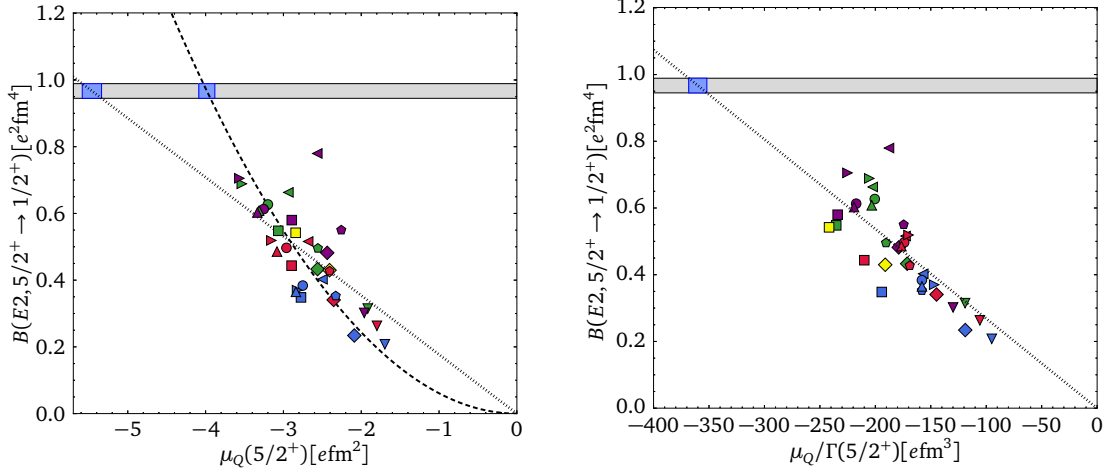


Figure 4: Correlation between $B(E2)$ and the quadrupole moment μ_Q . The IT-NCSM data is obtained with different $NN + 3N$ chiral EFT interactions: EM with cutoffs {400, 400, 500} MeV/c (square, diamond, triangle down), and EGM with cutoffs $(\Lambda_\chi/\bar{\Lambda}_\chi) = \{(450/500), (600/500), (550/600), (450/700), (600/700)\}$ MeV/c (triangle left, pentagon, circle, triangle right, and triangle up) with oscillator frequency $\hbar\Omega = 16$ MeV for all IT-NCSM calculations except for the diamond and triangle down data where $\hbar\Omega = 20$ MeV. Different colors denote different $N_{max} = 2$ (blue), 4 (red), 6 (green), 8 (violet), and 10 (yellow) values. Left panel: Rigid rotor model with quadratic fit of Q_t/Q_s ratio (dashed line, $\chi^2_{red} = 110$) and linear halo EFT fit of $\tilde{L}_{C02}^{(d)}$ with fixed γ_2 from experiment (dotted line, $\chi^2_{red} = 123$). Right panel: Linear halo EFT fit with $\gamma_0^2 - \gamma_2^2$ from IT-NCSM calculation and rescaled μ_Q/Γ (dotted line, $\chi^2_{red} = 80$), where $\Gamma = \gamma_0(3\gamma_0^2 + 9\gamma_0\gamma_2 + 8\gamma_2^2)^2 / (1 - r_0\gamma_0)/(\gamma_0 + \gamma_2)^6$ divides out dependence on γ_0 and γ_2 . The gray shaded area indicates the error band of the experimental $B(E2)$ [21]. The blue shaded area corresponds to the prediction for μ_Q .

out the data sets with exchanged ordering does not significantly improve the fit. The plot on the left side employs the experimental values for the neutron separation energy as input for γ_0 and γ_2 . For the plot on the right side, we use the excitation energy of the first excited state from the IT-NCSM to determine $\gamma_0^2 - \gamma_2^2$ and for γ_0 we use the experimental value.

From the left plot, we obtain $\mu_Q^{(d)} \approx -3.98(5)$ for the quadratic fit and $\mu_Q^{(d)} \approx -5.46(12)$ for the linear fit, where the uncertainties from $B(E2)$ are given in parenthesis. For both fits, $\tilde{L}_{C02}^{(d) LO} R_{core} \approx 10^{-3}$ which is very small. From the fits, we can not decide which scenario describes the IT-NCSM data more appropriately since both lead to similar reduced χ^2 values. The ratio $Q_{0,t}/Q_{0,s}$ should be equal to 1 for an ideal rigid rotor. Since the quadratic fit yields a ratio of $Q_{0,t}/Q_{0,s} \approx 0.5$, we assume that ^{15}C is not a good example of a rigid rotor. Perhaps for larger N_{max} values, and thus better converged results, the matching between fit curves and data points would improve.

In the linear case, the slope of the fit depends also on the neutron separation energies of both states, which differ for each data point from the IT-NCSM. From the excitation energy obtained in the IT-NCSM calculation, we know only the difference between the neutron separation energies of the ground and excited state. Thus one experimental input is still required to fix γ_0 and γ_2 from the IT-NCSM data, since we did not perform explicit calculations for ^{14}C . In the right plot of Fig. 4, we determine $\gamma_0^2 - \gamma_2^2$ from IT-NCSM data and take γ_0 from experiment. The reduced χ^2 value for the linear fit then slightly improves compared to the fit using experimental values only. This leads to $\mu_Q^{(d)} \approx -4.21(10)$, which is closer to the value from the quadratic fit. The deviations of the data points from the linear fit might decrease further if consistent values for both neutron separation energies could be extracted from the IT-NCSM.

However, within the 30% LO uncertainty from Halo EFT both values for $\mu_Q^{(d)}$ agree. Finally, we note that the linear correlation between the quadrupole moment and the E2 transitions strength also persists in NLO. A detailed discussion of the NLO corrections will be given in [35].

4. Conclusion

We have extended the halo EFT approach for the calculation of electric observables introduced in [13] to the $\frac{5}{2}^+$ excited state ^{15}C . In particular, we have developed a new power-counting scheme for shallow D -wave bound states which assumes $a_2 \sim R_{halo}^4 R_{core}$ and $r_2 \sim 1/(R_{halo}^2 R_{core})$ while all other parameters scale with R_{core} . This scheme differs from the general scheme proposed by Bedaque et al. in [4]. The Bedaque scheme requires only one fine tuning in the leading order parameter set, but further fine tunings appear through higher order power law divergences that have to be cancelled. Our scheme requires two fine tunings for the D -wave case, but is better adapted to the scale hierarchy in ^{15}C than the scheme of [4].

Using this scheme, we have computed the electric and quadrupole form factors of the excited state to LO and gave analytical expressions for the form factors. The hexadecupole form factor vanishes to this order. We find that for the D -wave, the local gauge-invariant operators become more important than in lower partial waves and counterterms are required in all form factors already at LO. This continues the trend, observed in [13], that the counterterms enter in lower orders at larger l . We have also computed the $B(E2)$ strength for the transition $\frac{1}{2}^+ \rightarrow \frac{5}{2}^+$ at LO and found that the first counterterm emerges at NLO. The emergence of counterterms in low orders limits the predictive power of halo EFT for D -waves. However,

this limitation can be overcome by considering universal correlations between observables as discussed below.

We emphasize that, up to this point, all our results are universal and not specific for ^{15}C . Considering now ^{15}C as an example, the lack of experimental data for the first excited $\frac{5}{2}^+$ state makes numerical predictions difficult. We cannot predict values for the charge radius and quadrupole moment at LO since the expressions (23) and (24) contain unknown counterterms. Nevertheless, we have determined a value for the quadrupole moment, $\mu_Q^{(d)} \approx -4.21(10)$, by exploiting the linear correlation between the reduced E2 transition strength $B(E2)$ and the quadrupole moment in our halo EFT and fitting the unknown counterterm to *ab initio* data from the IT-NCSM. These correlations are not obvious in *ab initio* approaches, since the separation of scales is not explicit in the parameters of the theory. This demonstrates the complementary character of halo EFT towards *ab initio* methods. In principle, the universal correlations allow to extract information even from unconverged *ab initio* calculations, since the correlations are universal. We have compared the linear halo EFT correlation to the quadratic correlation based on the simple rotational model by Bohr and Mottelson. The value for the quadrupole moment, $\mu_Q^{(d)} \approx -3.98(5)$, obtained from the quadratic correlation deviates from the linear result by 5% – 30% depending on the input used for $\gamma_0^2 - \gamma_2^2$. Within the accuracy of LO Halo EFT this is still consistent.

While there is a clear correlation in the *ab initio* data, there are also some outliers. In the case of the linear halo EFT correlation this could be due to the use of the experimental value of the ground state neutron separation energy γ_0 , which is presumably inconsistent with some of the *ab initio* data sets. Since the halo EFT correlation depends on the exact neutron separation energy of the two states, consistent values should be used. Better converged data sets and the future determination of the neutron separation energy directly from the IT-NCSM would help to clarify the situation. The explicit calculation of NLO corrections to the *D*-wave state observables will be presented in a future publication [35]. Moreover, we aim for the calculation of magnetic observables of the *D*-wave state, similar to the *S*-wave state considered in [19].

We thank L. Platter for discussions. This work has been supported by Deutsche Forschungsgemeinschaft through contract SFB 1245 and by the BMBF through contract no. 05P15RDFN1.

References

- [1] E. Braaten and H.-W. Hammer, Phys. Rept. **428** (2006) 259 [cond-mat/0410417].
- [2] A. Jensen, K. Riisager, D. V. Fedorov, E. Garrido, Rev. Mod. Phys. **76** (2004) 215.
- [3] C. Bertulani, H.-W. Hammer, U. van Kolck, Nucl. Phys. A **712** (2002) 37 [nucl-th/0205063].
- [4] P. F. Bedaque, H.-W. Hammer, U. van Kolck, Phys. Lett. B **569** (2003) 159 [nucl-th/0304007].
- [5] G. Hagen, P. Hagen, H.-W. Hammer and L. Platter, Phys. Rev. Lett. **111** (2013) 132501 [arXiv:1306.3661 [nucl-th]].
- [6] X. Zhang, K. M. Nollert and D. R. Phillips, Phys. Rev. C **89** (2014) no.5, 051602 [arXiv:1401.4482 [nucl-th]].
- [7] X. Zhang, K. M. Nollert and D. R. Phillips, Phys. Rev. C **89** (2014) 024613 [arXiv:1311.6822 [nucl-th]].
- [8] D. L. Canham and H.-W. Hammer, Eur. Phys. J. A **37** (2008) 367 [arXiv:0807.3258 [nucl-th]].
- [9] D. L. Canham and H.-W. Hammer, Nucl. Phys. A **836** (2010) 275 [arXiv:0911.3238 [nucl-th]].
- [10] J. Rotureau and U. van Kolck, Few Body Syst. **54** (2013) 725 [arXiv:1201.3351 [nucl-th]].
- [11] C. Ji, C. Elster and D. R. Phillips, Phys. Rev. C **90** (2014) 044004 [arXiv:1405.2394 [nucl-th]].
- [12] L. S. Brown and G. M. Hale, Phys. Rev. C **89** (2014) 014622 [arXiv:1308.0347 [nucl-th]].
- [13] H.-W. Hammer and D. R. Phillips, Nucl. Phys. A **865** (2011) 17 [arXiv:1103.1087 [nucl-th]].
- [14] H.-W. Hammer, C. Ji and D. R. Phillips, J. Phys. G **44** (2017) 103002 [arXiv:1702.08605 [nucl-th]].
- [15] E. Ryberg, C. Forssén, H.-W. Hammer and L. Platter, Phys. Rev. C **89** (2014) no.1, 014325 [arXiv:1308.5975 [nucl-th]].
- [16] E. Ryberg, C. Forssén, H.-W. Hammer and L. Platter, Annals Phys. **367** (2016) 13 [arXiv:1507.08675 [nucl-th]].
- [17] S. I. Ando, Int. J. Mod. Phys. E **25** (2016) 1641005 [arXiv:1512.07674 [nucl-th]].
- [18] G. Rupak, Int. J. Mod. Phys. E **25** (2016) 1641004.
- [19] L. Fernando, A. Vaghani and G. Rupak, arXiv:1511.04054 [nucl-th].
- [20] G. Rupak, L. Fernando and A. Vaghani, Phys. Rev. C **86** (2012) 044608 [arXiv:1204.4408 [nucl-th]].
- [21] F. Ajzenberg-Selove, Nucl. Phys. A **523** (1991) 1.
- [22] D. B. Kaplan, M. J. Savage and M. B. Wise, Phys. Lett. B **424** (1998) 390 [nucl-th/9801034].
- [23] D. B. Kaplan, M. J. Savage and M. B. Wise, Nucl. Phys. B **534** (1998) 329 [nucl-th/9802075].
- [24] R. Roth, Phys. Rev. C **79** (2009) 064324 [arXiv:0903.4605 [nucl-th]].
- [25] A. Bohr, B. R. Mottelson, Nuclear structure, Vol. II, World Scientific, Singapore (1975).
- [26] A. Calci and R. Roth, Phys. Rev. C **94** (2016) 014322 [arXiv:1601.07209 [nucl-th]].
- [27] S. R. Beane and M. J. Savage, Nucl. Phys. A **694** (2001) 511 [nucl-th/0011067].
- [28] U. van Kolck, Lect. Notes Phys. **513** (1998) 62 [hep-ph/9711222].
- [29] U. van Kolck, Nucl. Phys. A **645** (1999) 273 [nucl-th/9808007].
- [30] T. Nakamura, et al., Phys. Rev. C **79** (2009) 035805.
- [31] G. t’Hooft, Nucl. Phys. B **61** (1973) 455.
- [32] S. Weinberg, Phys. Rev. D **8** (1973) 3497.
- [33] J. Braun and H.-W. Hammer, Few Body Syst. **58** (2017) 94 [arXiv:1612.07689 [nucl-th]].
- [34] I. Angeli, K. Marinova, Atomic Data and Nuclear Data Tables **99** (2013) 69.
- [35] J. Braun, H.-W. Hammer, in preparation.
- [36] W. Greiner, D. A. Bromley, J. Maruhn, Nuclear Models, Springer, Berlin, Heidelberg (1996).
- [37] S. Typel and G. Baur, Nucl. Phys. A **759** (2005) 247 [nucl-th/0411069].
- [38] D. R. Entem and R. Machleidt, Phys. Rev. C **68** (2003) 041001 [nucl-th/0304018].
- [39] P. Navrátil, Few Body Syst. **41** (2007) 117 [arXiv:0707.4680 [nucl-th]].
- [40] E. Epelbaum, W. Glöckle and U. G. Meißner, Eur. Phys. J. A **19** (2004) 125 [nucl-th/0304037].
- [41] K. Hebeler and R. J. Furnstahl, Phys. Rev. C **87** (2013) 031302 [arXiv:1301.7467 [nucl-th]].
- [42] I. Tews, T. Krüger, K. Hebeler and A. Schwenk, Phys. Rev. Lett. **110** (2013) 032504 [arXiv:1206.0025 [nucl-th]].
- [43] T. Krüger, I. Tews, K. Hebeler and A. Schwenk, Phys. Rev. C **88** (2013) 025802 [arXiv:1304.2212 [nucl-th]].